International Journal of Heat and Mass Transfer 52 (2009) 2009–2017

Contents lists available at ScienceDirect

International Journal of Heat and Mass Transfer

journal homepage: www.elsevier.com/locate/ijhmt

Thermal performance of dimpled surfaces in laminar flows

Nian Xiao [a], Qiang Zhang [b], Phillip M. Ligrani [b,*], Rajiv Mongia [c]

[a] Department of Mechanical Engineering, University of Utah, Salt Lake City, UT 84112-9208, USA
[b] Department of Engineering Science, University of Oxford, Oxford OX1 3PJ, UK
[c] Intel Corporation, 2200 Mission College Blvd, Santa Clara, CA 95054-1549, USA

ARTICLE INFO

Article history:
Received 2 October 2007
Available online 26 December 2008

ABSTRACT

The present study provides data which illustrate the effects of an array of dimples on local and spatially-averaged surface Nusselt number distributions, as well as on friction factors in channels with *laminar flow*. Trends of spatially-averaged Nusselt numbers and friction factors are provided as they vary with dimple depth, channel height, Reynolds number from 260 to 1030, and the use of protrusions on the opposite channel wall. When compared with turbulent flow results, the present laminar data illustrate changes due to the absence of turbulence transport. For example, in contrast to turbulent flows, the present laminar flow data show that there is no overall benefit from the use of a top wall with protrusions. In addition, spatially-averaged Nusselt number ratios and friction factor ratios measured on a deep dimpled surface with a smooth top wall show trends which are opposite from ones observed in turbulent flows, since lower laminar heat transfer augmentations are present for smaller channel heights when compared at the same Reynolds number.

1. Introduction

Surface dimples produce substantial surface heat transfer augmentations with relatively small pressure drop penalties in internal passages. As such, arrays of surface dimples are useful for a variety of practical applications, such as electronics cooling, heat exchangers, turbine blade internal cooling passages, micro-scale passages, bio-medical devices, and combustion chamber liners. Of several early studies (mostly conducted in Russia), Murzin et al. [1] describe the flow over and within shallow spherical depressions and conclude that this flow is mostly symmetric, with stable re-circulatory flows inside of the depressions. Kesarev and Kozlov [2] present distributions of local heat transfer coefficients inside of a single hemispherical cavity and indicate that the convective heat transfer from the cavity is higher, especially on the downstream portion, than that from the surface of a plane circle of the same diameter as the cavity diameter. Afanasyev et al. [3] experimentally studied the heat transfer enhancement mechanism for flows in a dimpled channel with several different shapes. Enhancements of 30–40%, with pressure losses that are not increased appreciably relative to a smooth surface, are reported. Terekhov et al. [4] present experimental measurements of flow structure, pressure fields, and heat transfer in a channel with a single dimple on one surface. According to the authors, pressure losses increase (compared to a smooth wall) with an increase of cavity depth and decrease as the Reynolds number increases. Cavity heat transfer enhancements are also noted, especially for shallow holes, mainly as a result of an increase in heat transfer area and the changes to flow structure produced by the dimple.

More recent investigations conducted in the USA include the one described by Chyu et al. [5], who present local heat transfer coefficient distributions on surfaces imprinted with staggered arrays of two different shapes of concavities. Over a range of Reynolds numbers, enhancement of the overall heat transfer rate is about 2.5 times smooth surface values, and friction factors are about half the values produced by conventional rib turbulators. Moon et al. [6] give data that show that improvements in heat transfer intensification and pressure losses remain at approximately constant levels for different Reynolds numbers and channel heights.

Ligrani et al. [7] discuss flow structure and local Nusselt number variations in a channel with dimples and protrusions on opposite channel walls. Instantaneous flow visualization images and surveys of time-averaged flow structure show that the protrusions result in added vortical, secondary flow structures and flow mixing. As a result, local friction factors and Nusselt numbers are augmented compared to a channel with no protrusions on the top wall. Mahmood et al. [8] indicate that important Nusselt number variations are observed as the array of protrusions is changed with respect to the locations of the dimples. With protrusions, form drag and channel friction are increased. As a result, thermal performance parameters are then generally slightly lower when protrusions and dimples are employed, compared to a channel with a smooth-dimple arrangement. Ligrani et al. [9] report detailed flow structural characteristics, including

* Corresponding author.
E-mail address: p_ligrani@msn.com (P.M. Ligrani).

0017-9310/$ - see front matter © 2008 Elsevier Ltd. All rights reserved.
doi:10.1016/j.ijheatmasstransfer.2008.11.006

Nomenclature

A_d	dimple surface area
A_0	projected smooth surface area
D	dimple print diameter
D_h	channel hydraulic diameter
F	spatially-averaged channel friction factor
f_0	baseline friction factor measured in a channel with smooth surfaces and no dimples
FOM	figure of merit, $(Nu/Nu_0)/(f/f_0)^2$
H	channel height
h'	local heat transfer coefficient based on flat projected surface area, $\dot{Q}''_0/(T_w - T_{mx})$
h	spatially-averaged heat transfer coefficient based on flat projected surface area, $\dot{Q}''_0/(T_w - T_{mx})$
k	thermal conductivity
Nu'	local Nusselt number, $h'Dh/k$
Nu	spatially-averaged Nusselt number, hDh/k
Nu_0	baseline Nusselt number in a channel with smooth surfaces and no dimples
P	streamwise spacing of adjacent dimple rows
$\dot{Q}''_0$	surface heat flux
Re_H	Reynolds number based on channel height, $H\overline{U}/v$
S	streamwise spacing of every other dimple row
T_w	wall temperature
T_{mx}	local mixed-mean temperature
TPP	thermal performance parameter, $(Nu/Nu_0)/(f/f_0)$
$\bar{v}$	channel spatially-averaged velocity
X	streamwise coordinate measured from test section inlet
Y	normal coordinate measured from test surface dimple horizon
Z	spanwise coordinate measured from test section centerline

Greek symbols

v	kinematic viscosity
δ	dimple depth

behavior of the primary and secondary vortex pairs shed from the dimples on a channel surface. Flow structure characteristics above dimpled surface with different dimple depths in a channel are described by Won et al. [10].

Most existing archival papers which utilize dimpled surfaces consider turbulent flows at higher Reynolds numbers. Existing thermal performance data for dimpled surfaces in laminar flows are rare, even though such data are useful for applications such as electronic cooling, where lower Reynolds numbers and lower speeds are present. The present study is aimed at partially remedying this deficiency by providing a systematic set of data which illustrate the effects of dimples on local and spatially-averaged surface Nusselt number distributions, as well as on friction factors in channels with *laminar flow*. Of particular interest are the changes which occur because of the absence of turbulence transport. In some cases, vastly different trends are present as flow conditions are altered, or as some aspect of channel geometry is changed. Two different dimple depths and three channel heights are employed at Reynolds numbers based on channel height ranging from 260 to 1030. Also included are laminar flow experimental results, which illustrate the combined effects of dimples and protrusions as they are located on opposite channel walls.

2. Experimental apparatus and procedures

2.1. Flow channel and test surface

A schematic of the facility used for the present study is shown in Fig. 1. The air passes into a rectangular bell mouth inlet, followed by a honeycomb, two screens, and a two-dimensional nozzle with a contraction ratio of 10. This nozzles leads to a boundary layer bleed-off plenum, followed by an inlet duct, the test section, and the downstream duct. The channel heights of all three ducts are adjustable by moving the duct top plates. The test section is 411 mm in width and 1219 mm in length. A series of two plenums (0.9 m square and 0.75 m square) are installed between the downstream duct and a 102 mm inner diameter pipe, which is then connected to the intake of an ILG Industries 10P type centrifugal blower. An ASME standard orifice plate and a Setra Model 267 differential pressure transducer are employed to measure the air mass flow rate through the pipe (and the test section as well).

Fig. 2a presents geometric details of the dimpled test surface employed in the test section. In the present study, a total of 29 rows of dimples are employed in the streamwise direction, with 4 or 5 dimples in each row. The dimples are positioned on the surface in a staggered array. The dimpled test surfaces are manufactured by vacuum forming acrylic sheets over molds with shapes designed to produce arrays of protrusions or dimples with the appropriate spacings, depth, and height, as required. Also identified in Fig. 2a is the test section coordinate system employed for the study. Note that the y-coordinate is normal from the test surface. Fig. 2b shows the individual dimple geometry details for deep and shallow dimples investigated in the present study. For one complete period of dimpled-surface geometry, the area ratios between dimpled and smooth surface for the deep and shallow dimples are 1.216 and 1.024, respectively. Ligrani et al. [7] and Mahmood et al. [8] present additional details on the dimpled test surfaces employed in the present study.

In addition to a smooth test section (for baseline data), four different channel configurations are employed in the present study, as shown in Fig. 3. The first configuration has a dimpled bottom surface and a smooth top surface, and the second configuration has protrusions on the top wall and dimples on the bottom surface, with the dimples and protrusions aligned with each other. The top-dimpled protrusion pattern is shifted ½ dimple print diameter and one print diameter for the other two configurations. The local reductions in flow cross-section area for these different configurations are evident in Fig. 3a–d.

All exterior surfaces of the facility (between the heat exchanger and test section) are insulated with 2–3 layers of 2.54 cm thick,

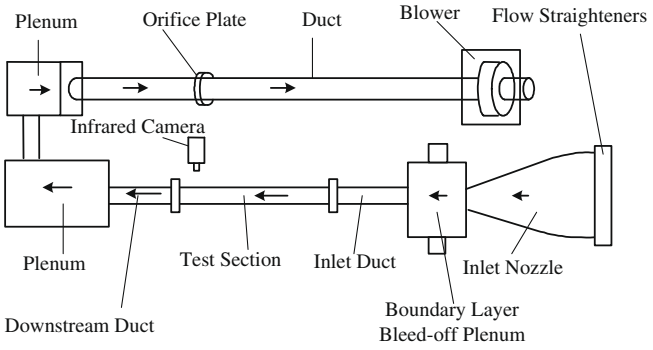

Fig. 1. Schematic diagram of the experimental apparatus.

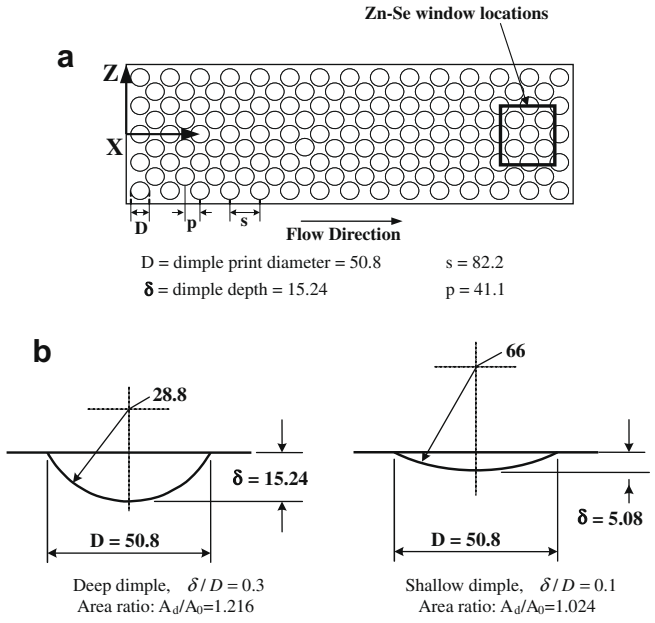

Fig. 2. Schematic diagrams of: (a) dimpled test surface with 29 streamwise staggered rows of dimples, and (b) individual dimple geometry details. All dimensions are given in mm.

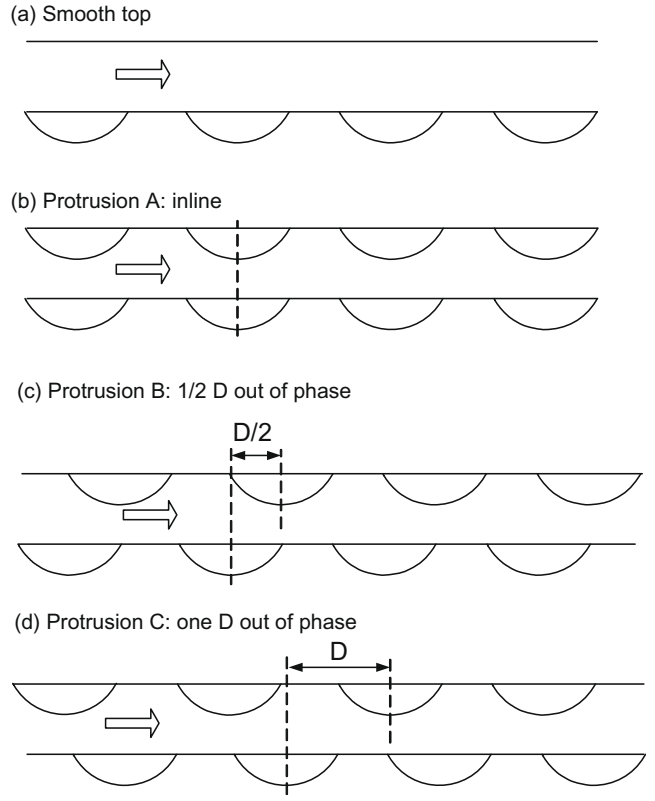

Fig. 3. Schematic diagrams of different channel configurations.

Elastomer Products black neoprene foam insulation (k = 0.038 W/mK) to minimize heat losses. Calibrated copper–constantan thermocouples are located between the three layers of insulation located around the entire test section to determine conduction losses. The dimpled test surfaces are made of 3.2 mm thick acrylic. Acrylic is chosen because of its low thermal conductivity (k = 0.16 W/mK at 20 °C) to minimize streamwise and spanwise conduction along the test surface, and thus minimize "smearing" of spatially-varying temperature gradients along the test surface. Between the first layer and bottom dimpled test surface is a custom-made Electrofilm etched-foil heater (encapsulated between two thin layers of Kapton) to provide a constant heat flux boundary condition on the bottom dimpled test surface. This custom-made heater is designed and constructed so that it follows the convex contour of the test surface behind each dimple. The power to the foil heater is controlled and regulated using a DC power supply. To determine the surface heat flux (used to calculate heat transfer coefficients and local Nusselt numbers), the total convective power level, provided by the etched foil heater, is divided by the flat, projected test surface area corresponding to that foil heater. Energy balances, performed on the heated test surface, then allow determination of local magnitudes of the convective heat flux.

2.2. Infrared thermography for local Nusselt number measurement

Spatially-resolved temperature distributions along the bottom test surface are determined using infrared imaging in conjunction with thermocouples, energy balances, digital image processing, and in situ calibration procedures.

To accomplish this, the infrared radiation emitted by the heated interior surface of the channel is captured using a FLIR ThermoVision A20 M Infrared Camera, which operates at infrared wavelengths from 7.5 to 13 μm. The camera views the test surface through a custom-made, zinc–selenide window (which transmits infrared wave lengths between 6 and 17 μm) located on the top wall of the downstream region of the test section, as shown in Fig. 2a. Note that all results given in the present paper are obtained at the same location which is just above the 26th to 29th rows of dimples downstream from the leading edge of the test surface. This is equivalent to 13–14 full periods of dimple test pattern in the streamwise direction, which means that the thermal and velocity flow fields are fully developed where the dimpled-surface heat transfer measurements are obtained.

The bottom dimpled acrylic surface contains 12 copper–constantan thermocouples in the infrared field viewed by the camera. A schematic diagram of dimpled surface viewed by the infrared camera through the zinc–selenide window is presented in Fig. 4. Marked locations correspond to the locations of the thermocouple junctions in this portion of the bottom surface. Each of these thermocouples is located 0.051 cm just below this surface to provide measurements of local surface temperatures, after correction for thermal contact resistance and temperature drop through the 0.051 cm thickness of acrylic. Temperatures, measured using these thermocouples are used to perform the in situ calibrations simultaneously as the radiation contours from surface temperature variations are recorded. The exact spatial locations and pixel locations of these thermocouple junctions and the coordinates of a 12.7 cm by 12.7 cm field of view are known from calibration maps obtained prior to measurements. During each test, the IR camera is focused, and rigidly mounted and oriented relative to the test surface in the same way as when radiation contours are captured. Because the calibration data depend strongly on camera adjustment, the same brightness, contrast, and aperture camera settings are used to obtain the experimental data. The in situ calibration approach rigorously and accurately accounts for these variations.

Gray scale images from the infrared camera are transferred into a Dell Precision PC computer. This final data set is then imported into Matlab software to convert the gray scale values to local temperature values based upon the calibration curve generated from each test.

The mixed-mean stagnation temperature of the air entering the test section is measured at the inlet cross-section. Magnitudes of the local mixed-mean temperatures at different locations through

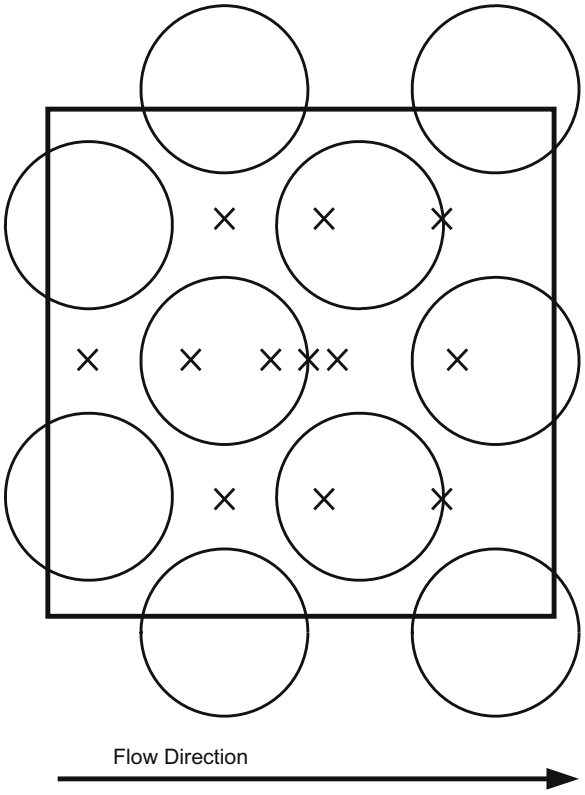

Fig. 4. Schematic diagram of dimpled surface viewed by the infrared camera through the zinc-selenide window. Marked locations correspond to the locations of the thermocouple junctions in this portion of the bottom dimpled surface. Each circle denotes a dimple, square box illustrates the infrared camera field of view.

the test section are then determined using energy balances and the mixed-mean temperature at the inlet of the test section. Because of the way in which it is measured, this inlet temperature is also a stagnation value. The thermal conductivity used to determine local Nusselt numbers is based on this inlet stagnation temperature. Mixed-mean temperatures, determined from temperatures measured at the exit of the duct, match values determined from energy balances within a few percent for all experimental conditions investigated. All measurements are obtained when the test facility is at steady-state, achieved when each of the temperature readings from the thermocouples and the infrared camera vary by less than 0.1 °C over a 10 min period.

2.3. Friction factor measurement

Wall static pressures are measured using static pressure taps along the test section simultaneously as the heat transfer measurements are conducted. The pressure taps are located on the test section side walls. Friction factors are determined from streamwise pressure gradient magnitudes. Pressures from the wall pressure taps are measured using Setra Model 267 differential pressure transducers. Voltage signals from the thermocouples and pressure transducers are captured by using a National Instruments NI 4351 high precision data acquisition card.

2.4. Experimental uncertainty estimates

Uncertainty estimates are based on 95% confidence levels, and determined using procedures described by Kline and McClintock [11] and Moffat [12]. Uncertainty of temperatures measured with thermocouples is ±0.15 °C. Spatial and temperature resolutions achieved with the infrared imaging are about 0.5 mm and 0.8 °C, respectively. This magnitude of temperature resolution is due to uncertainty in determining the exact locations of thermocouples with respect to pixel values used for the in situ calibrations. Local Nusselt number uncertainty is then about ±6.8%. Corresponding Nusselt number ratio uncertainty is about ±0.19 (for a ratio of 2.00), or ±9.6%. Note that all uncertainties of local Nusselt numbers consider variations of surface heat flux which may be present due to small changes of the thickness of the acrylic which comprises the dimpled test surface.

3. Experimental results and discussion

A summary of all of the experimental conditions employed in the present study is given in Table 1.

3.1. Baseline Nusselt numbers and friction factors

Fig. 5 presents baseline Nusselt numbers and baseline friction factors over a range of Reynolds numbers, which are measured with smooth channel surfaces and a constant heat flux boundary condition on the heated surface. The aspect ratio of the channel used to obtain these data is 16. These baseline data are in agreement with laminar flow numerical predictions from FLUENT. The Nu_0 data in Fig. 5a decrease with x/D such that higher Nu_0 are present as Re_H increases at each x/D, to approach the fully developed behavior at $x/D > 20$. The data in Fig. 5b lie just above the fully developed friction factor value at each Reynolds number, which is consistent with developing flow behavior. As such, the Nu_0 and f_0 trends shown by these data provide validation of the experimental apparatus and procedures used to obtain the experimental data.

3.2. Local Nusselt number distributions

Nusselt number ratios, friction factor ratios, and associated quantities measured on deep dimpled surfaces with $\delta/D = 0.3$ and a smooth top wall are presented in Figs. 6–9. Fig. 6 presents local Nusselt number ratio Nu/Nu_0 distributions for 25.4 mm channel height, $Re_H = 453.5$, and $H/D = 0.5$. Note that the Nu_0 values used to normalized these data are obtained at the same Re_H and with a channel having the same aspect ratio as the Nu data. In some cases, baseline Nu_0 values are determined using numerical predictions. The bulk flow direction in Fig. 6 is from left to right in the direction of increasing X/D. Local values are lowest in the upstream halves of the dimples. Each of these is positioned beneath a region of re-circulating flow, where advection velocities in the flow located adjacent to the surface are very low. Nusselt number ratios then increase progressively along the dimpled surface. Values then become highest on the flat surfaces just downstream of each dimple. This is mostly due to shear layer re-attachment, and the extra advection induced by the secondary flows associated with the vortices which are shed from the dimples. Such events then continue to enhance local heat transfer levels upstream of adjacent dimples which are located just downstream. Similar trends are evident for all H/D and Re_H values investigated, provided that top wall is smooth, $\delta/D = 0.3$, and the flow is laminar. Such laminar flow trends are in approximate agreement with turbulent flow results presented by Moon et al. [6], and Mahmood et al. [8]. The most important differences are (i) the position of the Nusselt number augmentation region, which is often present further into the dimples when the flow is turbulent, and (ii) Nusselt number enhancements near dimple edges from edge vortex pairs are more pronounced when the flow is turbulent. This spatially-averaged Nusselt number ratio Nu/Nu_0, determined from the laminar flow data in Fig. 6 over one complete period of dimple surface geometry, is 2.09.

Table 1
Experimental conditions

Dimple depths	Deep dimple, shallow dimple (see Fig. 2) $\delta/D = 0.1, 0.3$
Channel heights H	25.4 mm, 19.1 mm, 12.7 mm $H/D = 0.5, 0.375, 0.25$
Top wall configurations	Smooth top, protrusion A, B, C (see Fig. 3)
Reynolds numbers	Four Reynolds numbers for each configuration (ranging from 260 to 1030)

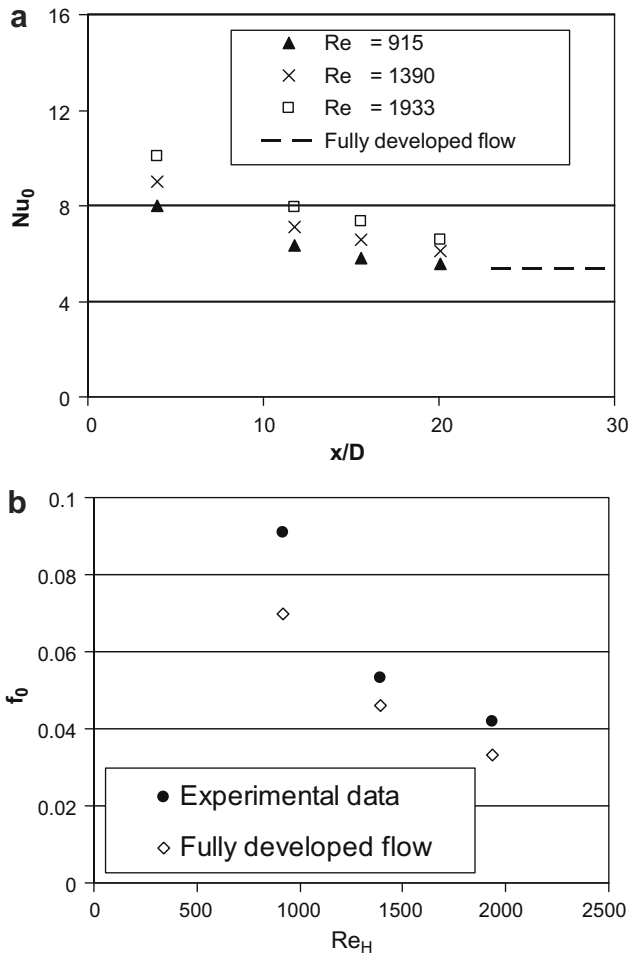

Fig. 5. Smooth channel baseline experimental results: (a) Nusselt number variation with X/D, and (b) friction factor variation with Reynolds number.

3.3. Spatially-averaged Nusselt number ratios and friction factor ratios, heated dimple surface – smooth top wall

Figs. 7 and 8 present spatially-averaged Nusselt number ratios and friction factor ratios measured on a deep dimpled surface ($\delta/D = 0.3$) with a smooth top wall, for different channel heights and different Reynolds numbers. Each spatially-averaged value is determined over one complete period of dimple surface geometry, using results like the ones presented in Fig. 6. As Reynolds number increases, both Nusselt number ratio and friction factor ratio increase for each H/D value. Note how Nu/Nu_0 and f/f_0 values from both Figs. 7 and 8 appear to approximately approach unity as the Reynolds numbers decreases. Trends of the Nusselt number ratio data with H/D in Fig. 7 are opposite from ones observed in turbulent flows since lower laminar heat transfer augmentations are present for smaller channel heights (when compared at the same Re_H). In contrast, the friction factor ratio data in Fig. 8 show only

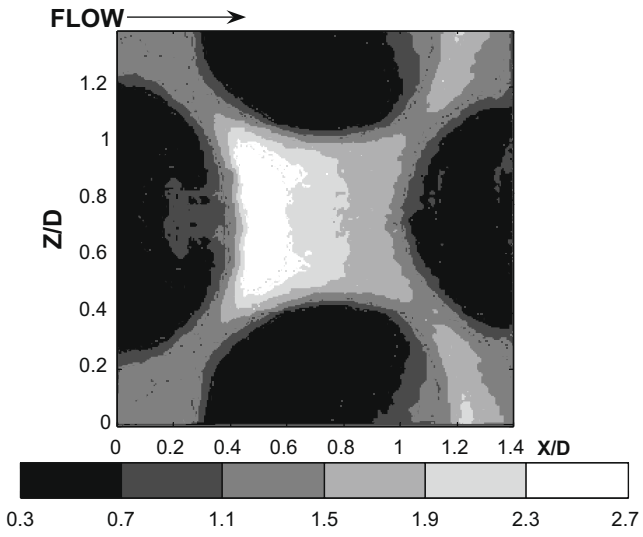

Fig. 6. Local Nusselt number ratio Nu'/Nu_0 distribution for deep dimples, $\delta/D = 0.3$, $H/D = 0.5$, $V = 0.306$ m/s, $Re_H = 453.5$, $Nu/Nu_0 = 2.09$.

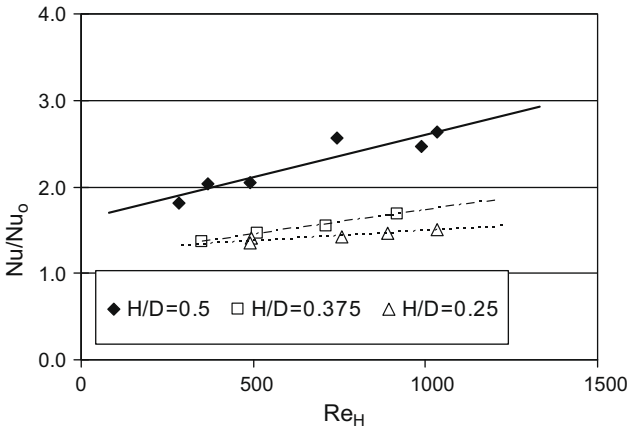

Fig. 7. Nusselt number ratio variation for the channel configuration of heated dimple bottom surface and smooth top with three different channel heights over a range of Reynolds numbers for deep dimples and $\delta/D = 0.3$.

small variations with H/D but increase with Reynolds number for each value of H/D and δ/D, a trend which is also observed when the flow over such a dimpled surface is fully turbulent [8]. Note that the baseline Nu_0 values used to normalized the data in Figs. 7 and 8 (as well as the data in Figs. 9–17) are obtained at the same Re_H and with a channel having the same aspect ratio as the dimpled surface Nu data.

Fig. 9a and b show how the globally-averaged dimpled channel thermal performance parameter, given by $TPP = (Nu/Nu_0)/f/f_0)$, and the figure of merit, given by $FOM = (Nu/Nu_0)/(f/f_0)^2$, respectively, vary with Reynolds number Re_H for deep dimples with $\delta/D = 0.3$, a smooth top wall, and three different channel heights. The first of these parameters is sometimes referred to an as Reynolds analogy thermal performance parameter. The figure of merit (FOM) provides comparisons between heat transfer augmentation and a pressure drop penalty quantity. Fig 9a and b show that higher H/D values and lower Reynolds numbers generally produce better overall thermal performance for these particular dimpled channel configurations. As Reynolds numbers increase above 500, the FOM values drop to less than one, which means unacceptably large values of the drop penalty quantity $(f/f_0)^2$.

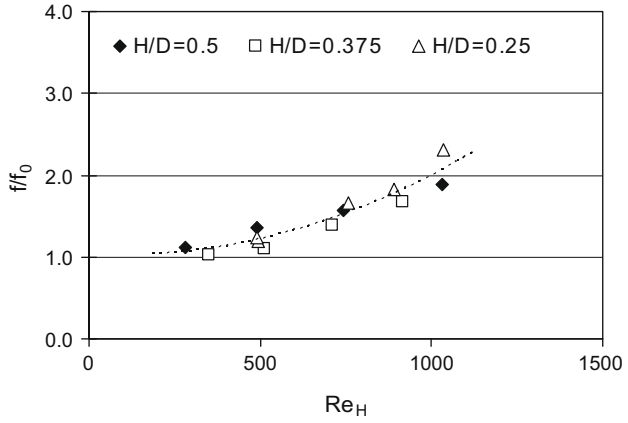

Fig. 8. Friction factor ratio variation for the channel configuration of heated dimple bottom surface and smooth top with three different channel heights over a range of Reynolds numbers for deep dimples and $\delta/D = 0.3$.

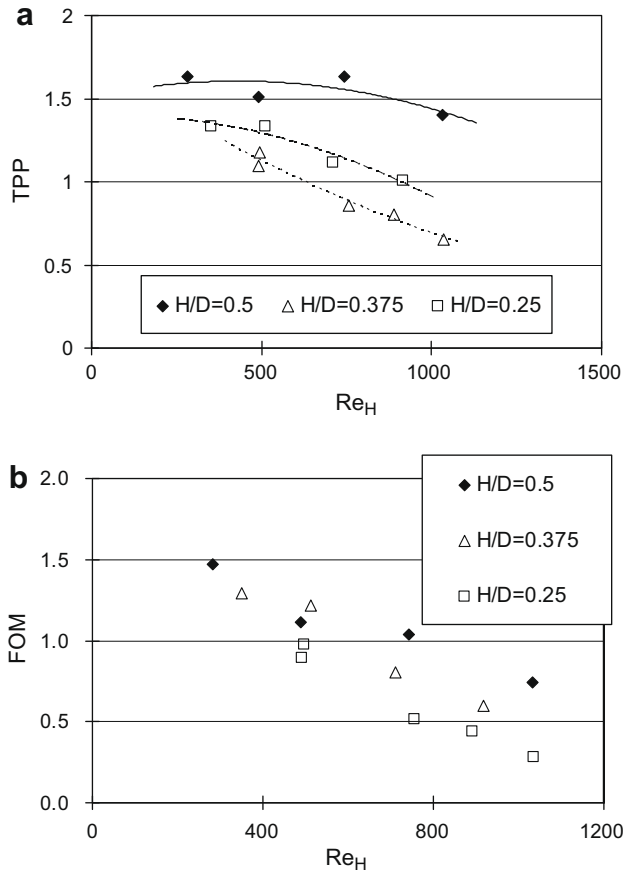

Fig. 9. (a) Thermal performance parameter (*TPP*) and (b) figure of merit (*FOM*) variations with Reynolds number for the channel configuration of heated dimple bottom/smooth top with three different channel heights for deep dimples and $\delta/D = 0.3$.

Figs. 10 and 11 again present experimental data for channels with smooth top surfaces and dimpled bottom surfaces. Here, data are given for *H*/*D* of .25, .375, and .5, and for δ/D of 0.1 and 0.3. These data are well correlated using equations having the following forms

$$Nu/Nu = 0.9583\mathrm{Re}_H^{0.23}\left(\frac{H}{D}\right)^{0.53}\left(\frac{\delta}{D}\right)^{0.19} - 0.1977$$

$$f/f_0 = 0.0259\mathrm{Re}_H^{0.47}\left(\frac{H}{D}\right)^{-0.33}\left(\frac{\delta}{D}\right)^{-0.66} - 0.247$$

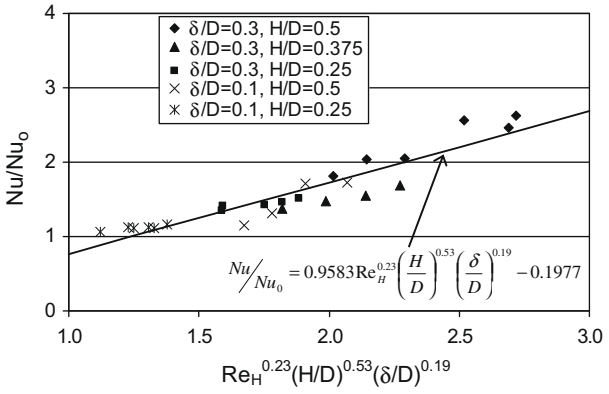

Fig. 10. Nusselt number ratio correlation for the channel configuration of heated dimple bottom/smooth top for shallow and deep dimples.

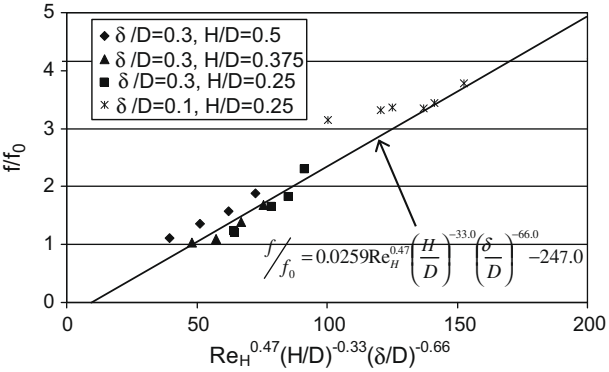

Fig. 11. Friction factor ratio correlation for the channel configuration of heated dimple bottom/smooth top for shallow and deep dimples.

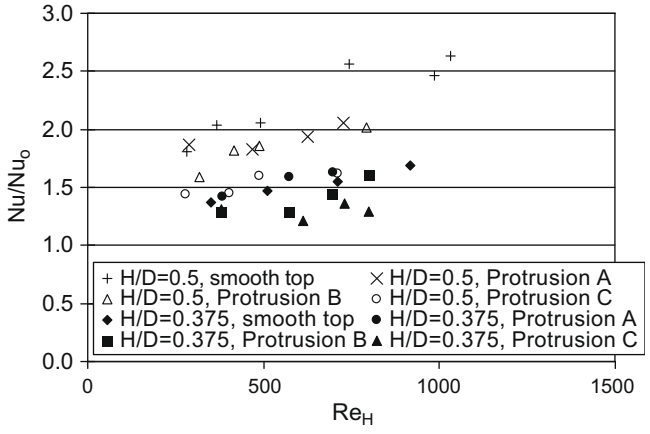

Fig. 12. Nusselt number ratio variation with Reynolds number for different channel top configurations with heated deep dimple bottom surface for deep dimples and $\delta/D = 0.3$.

The maximum deviation of the Nu/Nu_0 equation from the experimental data in Fig. 10 is about 18%. The maximum deviation of the f/f_0 equation from the experimental data in Fig. 11 is about 21%.

3.4. Spatially-averaged Nusselt number ratio and friction factor ratios, heated dimple surface – protrusion top wall

Spatially-averaged Nusselt number ratios, friction factor ratios, thermal performance parameter magnitudes, and figure of merit

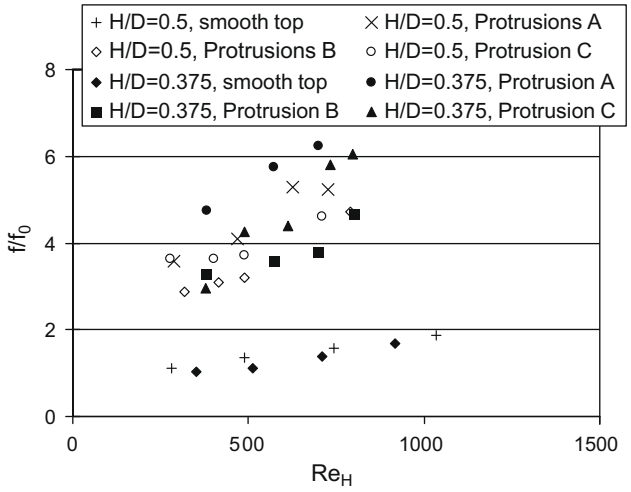

Fig. 13. Friction factor ratio variation with Reynolds number for different channel top configurations with heated deep dimple bottom surface and $\delta/D = 0.3$.

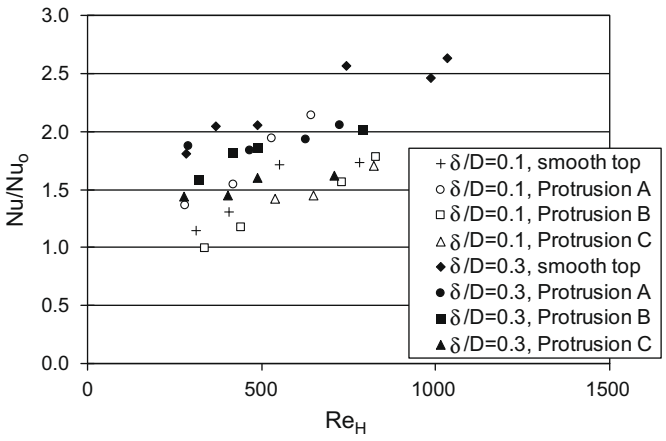

Fig. 15. Nusselt number ratio variation with Reynolds number for different channel top configurations, shallow and deep dimples, and $H/D = 0.5$.

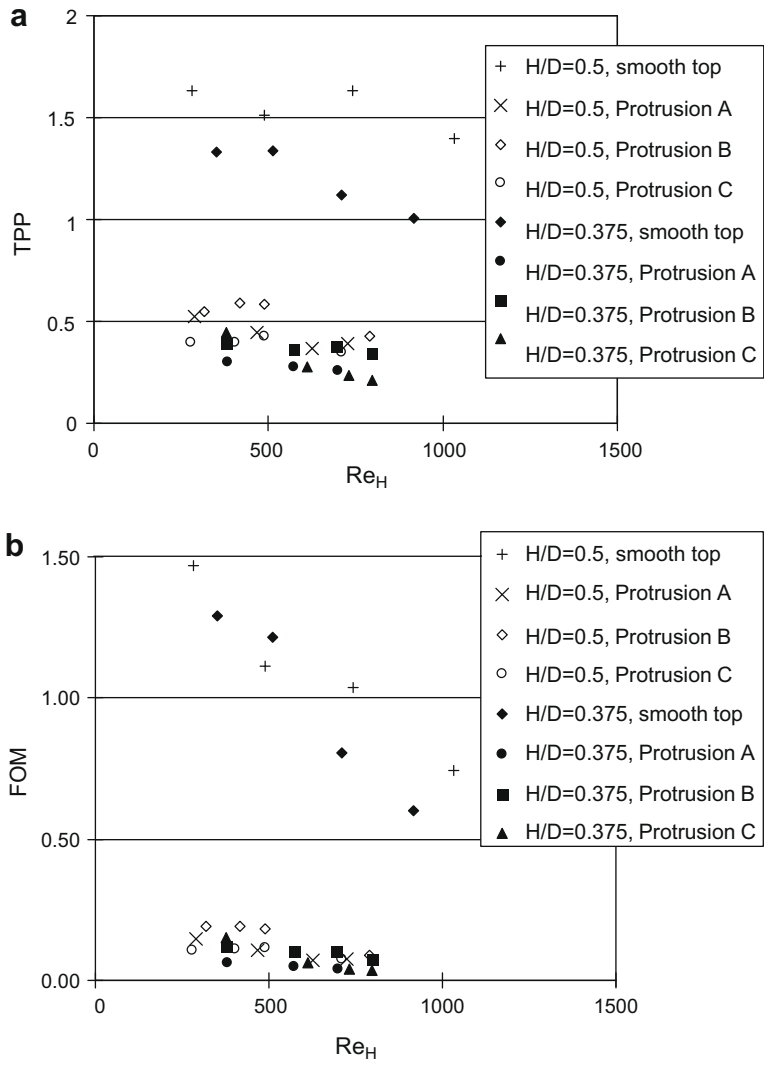

Fig. 14. (a) Thermal performance parameters and (b) figure of merit variations with Reynolds number for different channel top configurations, deep dimples, and $\delta/D = 0.3$.

magnitudes are presented in Figs. 12–17 from measurements on heated dimpled surfaces with an array of protrusions on the top channel wall. Here, spatially-averaged Nusselt numbers are not obtained using infrared thermography since it is not possible to fab-

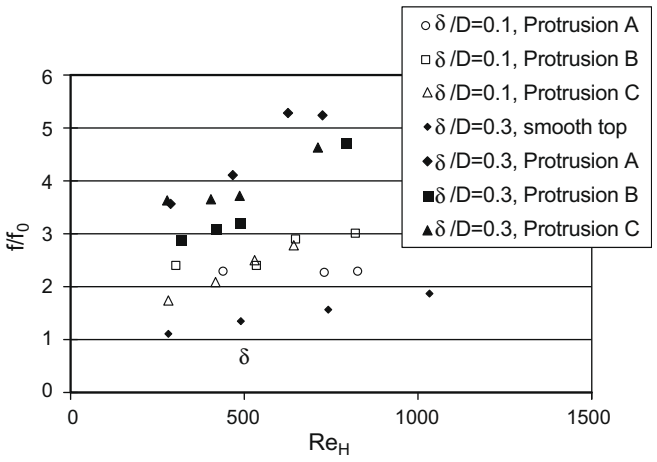

Fig. 16. Friction factor ratio variation with Reynolds number for different channel top configurations, shallow and deep dimples, and $H/D = 0.5$.

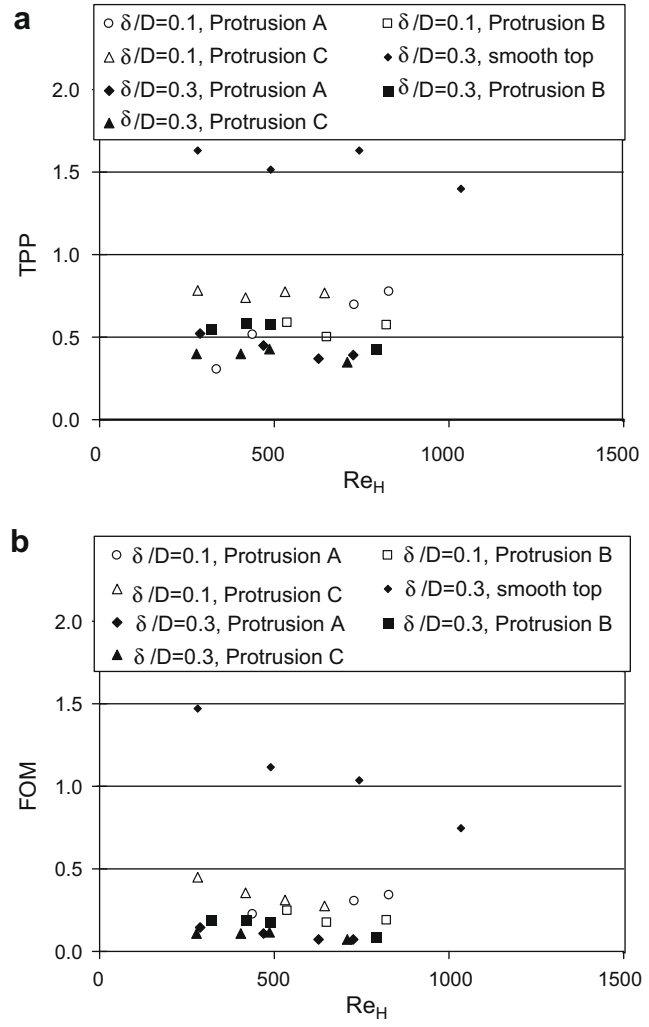

Fig. 17. (a) Thermal performance parameter (*TPP*) and (b) figure of merit (*FOM*) variations with Reynolds number for different channel top configurations, shallow and deep dimples, and $H/D = 0.5$.

ricate different zinc-selenide windows with protrusions for installation onto the channel top wall (to allow infrared camera viewing of the bottom test surface). Instead, local thermocouples readings are employed to measure local surface temperatures, which are used to determine local Nusselt numbers for each configuration. Spatially-averaged Nusselt numbers are then determined from these local Nusselt number distributions. When the top surface of the channel is smooth, differences between spatially-averaged Nusselt numbers measured using local thermocouple measured temperature readings are within about ±2% of spatially-averaged Nusselt numbers determined from spatially-resolved data measured using infrared thermography. Nusselt number ratio data presented in this section thus provide representative information of the effects of protrusions on dimpled-surface Nusselt numbers, but with slightly higher experimental uncertainty magnitudes compared to data from the previous section.

The data in Figs. 12–14 are given for deep dimples, deep protrusions, H/D of 0.375 and 0.5, and different arrangements of the protrusions relative to the dimples. Fig. 12 shows that protrusions generally result in lower Nusselt number ratio enhancements (on the dimpled surface) compared to arrangements with smooth top walls. In contrast, Ligrani et al. [7] show that higher dimpled-surface heat transfer enhancements are produced by protrusions when the flows are fully turbulent. These differences are due in part to the wakes, boundary layer skewing, flow re-circulation zones, and shear layer re-attachments, which are created by the protrusions, and result in increased mixing and three-dimensional thermal and momentum transport when the flow is fully turbulent. However, when the flow is laminar, the overall influences of these phenomena are detrimental to Nusselt number augmentations because of the absence of turbulent transport and mixing, and the insulating influences of the low-speed flow re-circulation zones which are located downstream of each protrusion. The data in Figs. 12 and 13 show how such phenomena produced by protrusions affect surface Nusselt number distributions on the opposite dimpled wall of the channel. The overall effect is suppression of the flow phenomena which are produced by an array of dimples which augment surface Nusselt numbers in laminar flows.

As mentioned previously, Fig. 3 shows the different protrusion arrangements A, B, and C which are employed. Fig. 12 shows that protrusion arrangement A, which has an aligned top and bottom dimple geometry, provides slightly higher Nusselt number ratios compared to results from protrusion configurations B and C. The laminar flow friction factor ratio data in Fig. 13 show similar trends with respect to protrusion configurations A, B, and C. However, in contrast to the results shown in Fig. 12, the protrusion f/f_0 data in Fig. 13 are generally higher than data obtained with a smooth top wall, when compared at a particular Reynolds number, Re_H. The same qualitative data trends are present in passages with turbulent flows and protrusions and dimples [7], which is consistent with increased pressure drops resulting from protrusion form drag.

Figs. 14a and b show the thermal performance parameter and figure of merit, respectively, as they vary with Reynolds number, also for deep dimples, deep protrusions, H/D of 0.375 and 0.5, and different arrangements of the protrusions relative to the dimples. The most important conclusion from these data is that the highest *TPP* and *FOM* values are present with a smooth top wall at any particular Re_H value, which means that there is no overall benefit from the use of a top wall with protrusions, provided the flow is fully laminar. When the different protrusion arrangements are considered, configuration Protrusion B, in which the protrusions are shifted $1/2D$ relative to the top dimples, provides slightly better thermal performance than the other protrusion arrangements A and C for $H/D = 0.375$ and $H/D = 0.5$.

Figs. 15–17 compare data from several channel configurations: (i) smooth top, shallow dimples $\delta/D = 0.1$, (ii) shallow protrusions, shallow dimples $\delta/D = 0.1$, (iii) smooth top, deep dimples $\delta/D = 0.3$, and (iv) deep protrusions, deep dimples $\delta/D = 0.3$. When compared

at a particular laminar Reynolds number Re_H, Fig. 15 shows that deep protrusion/deep dimple data produce higher Nusselt number augmentations than the shallow protrusion/shallow dimple data. Similar trends are present when the channel flows are fully turbulent. However, the laminar data in Fig. 15, which are obtained with a smooth top wall, show higher Nusselt number augmentations than the protrusion A, B, and C configurations (when compared at a particular Re_H), a trend which is different from the ones which are present when the channel flows are fully turbulent. The friction factor ratio data, presented in Fig. 16, on the other hand, show similar trends as observed in turbulent flows, with higher f/f_0 values as protrusions are added to the top wall, and higher f/f_0 values as the depths of the dimples and heights of the protrusions increase. The *TPP* and *FOM* data in Fig. 17a and b, respectively, show that when the dimple/protrusion data are considered, the δ/D=0.1 data generally show better overall performance than the δ/D=0.3 data, when compared at a particular Reynolds number Re_H.

4. Summary and conclusions

The present study provides a systematic set of data which illustrate the effects of an array of dimples on local and spatially-averaged surface Nusselt number distributions, as well as on friction factors in channels with *laminar flow*. Two dimple depths and three channel heights are employed over Reynolds numbers ranging from 260 to 1030. Also included are laminar flow experimental results which provide information on the combined effects of dimples and protrusions, as they are placed on opposite channel walls.

When compared with turbulent flow results [1–10], the present laminar data illustrate changes due to the absence of turbulence transport. For example, local laminar flow Nusselt number ratios at Re_H = 453.5, and H/D = 0.5 (with a smooth top wall) are different from turbulent results because Nusselt number augmentation regions do not extend as far into the dimples, and because Nusselt number enhancements near dimple edges from edge vortex pairs are more pronounced when the flow is turbulent. In addition, spatially-averaged Nusselt number ratios and friction factor ratios measured on a deep dimpled surface (δ/D = 0.3) with a smooth top wall show trends which are opposite from ones observed in turbulent flows, since lower laminar heat transfer augmentations are present for smaller channel heights (when compared at the same Re_H). In contrast, friction factor ratio data show only small variations with H/D but increase with Reynolds number for each value of H/D and δ/D, a trend which is also observed when the flow over such a dimpled surface is fully turbulent.

When protrusion top-wall data with laminar flow are considered, lower Nusselt number ratio enhancements are present on the dimpled surface compared to arrangements with smooth top walls. In contrast, Ligrani et al [7] show that higher dimpled-surface heat transfer enhancements are produced when protrusions are present when the flows are fully turbulent. The associated thermal performance parameter and figure of merit data show that the highest values are present with a smooth top wall at any particular Re_H value, which means that there is no overall benefit from the use of a top wall with protrusions, provided the flow is fully laminar. These same parameters show that deep dimple surfaces generally produce lower overall performance at a particular Reynolds number than shallow dimple surfaces, provided the flows are laminar and protrusions are present on the opposite wall.

The observed differences between laminar and turbulent flows are due in part to the wakes, boundary layer skewing, flow re-circulation zones, and shear layer re-attachments, which are created by the protrusions, and result in increased mixing and three-dimensional thermal and momentum transport when the flow is fully turbulent. However, when the flow is laminar, the overall influences of these phenomena are detrimental to Nusselt number augmentations measured on opposite dimpled surfaces because of the absence of turbulent transport and mixing. The low-speed flow re-circulation zones and other secondary flows produced by the protrusion array thus appear to partially suppress those laminar flow phenomena from dimples which are responsible for augmentation of surface Nusselt numbers.

Acknowledgments

The work presented in this paper was sponsored and supported by Intel Corporation.

References

[1] V.N. Murzin, S.S. Stoklitskii, A.P. Chebotarev, Creation of solitary vortices in a flow around shallow spherical depressions, Soviet Tech. Phys. Lett. 12 (11) (1986) 547–549.
[2] V.S. Kesarev, A.P. Kozlov, Convective heat transfer in turbulized flow past a hemispherical cavity, Heat Transfer Res 25 (2) (1993) 156–160.
[3] V.N. Afanasyev, Y.P. Chudnovsky, A.I. Leontiev, P.S. Roganov, Turbulent flow friction and heat transfer characteristics for spherical cavities on a flat plate, Exp Therm Fluid Sci 7 (1993) 1–8.
[4] V.I. Terekhov, S.V. Kalinina, Y.M. Mshvidobadze, Flow structure and heat transfer on a surface with a unit hole depression, Russ. J. Eng. Therm. 5 (1995) 11–33.
[5] M.K. Chyu, Y. Yu, H. Ding, J.P. Downs, F.O. Soechting, Concavity enhanced heat transfer in an internal cooling passage, in: ASME Congress and Exposition, Orlando, Florida, 1997.
[6] H.K. Moon, T. O'Connell, B. Glezer, Channel height effect on heat transfer and friction in a dimpled passage, J. Eng. Gas Turb. Power 122 (2000) 307–313.
[7] P.M. Ligrani, G.I. Mahmood, J.L. Harrison, C.M. Clayton, D.L. Nelson, Flow structure and local Nusselt number variations in a channel with dimples and protrusions on opposite walls, Int. J. Heat Mass Transfer 44 (23) (2001) 4413–4425.
[8] G.I. Mahmood, M.Z. Sabbagh, P.M. Ligrani, Heat transfer in a channel with dimples and protrusions on opposite walls, AIAA J. Thermophys. Heat Transfer 15 (3) (2001) 275–283.
[9] P.M. Ligrani, J.L. Harrison, G.I. Mahmood, M.L. Hill, Flow structure due to dimple depressions on a channel surface, Phys. Fluids 13 (11) (2001) 3442–3451.
[10] S.Y. Won, Q. Zhang, P.M. Ligrani, Comparison of flow structure above dimpled surfaces with different dimple depths in a channel, Phys. Fluids 17 (4) (2005) 0451051–0451059.
[11] S.J. Kline, F.A. McClintock, Describing uncertainties in single sample experiments, Mech. Eng. 75 (1953) 3–8.
[12] R.J. Moffat, Describing the uncertainties in experimental results, Exp. Therm. Fluid Sci. 1 (1) (1988) 3–17.